

Supersymmetric particle mass measurement with invariant mass correlations

Davide Costanzo* and **Daniel R. Tovey†**

*Department of Physics and Astronomy,
University of Sheffield, Hounsfield Road,
Sheffield S3 7RH, UK*

ABSTRACT: The kinematic end-point technique for measuring the masses of supersymmetric particles in R-Parity conserving models at hadron colliders is re-examined with a focus on exploiting additional constraints arising from correlations in invariant mass observables. The use of such correlations is shown to potentially resolve the ambiguity in the interpretation of quark+lepton end-points and enable discrimination between sequential two-body and three-body lepton-producing decays. The use of these techniques is shown to improve the SUSY particle mass measurement precision for the SPS1a benchmark model by at least 20-30% compared to the conventional end-point technique.

KEYWORDS: SUSY, fit, end-point.

*davide.costanzo@cern.ch

†daniel.tovey@cern.ch

Contents

1. Introduction	1
2. Kinematic constraints from three-step sequential two-body decay chains	2
2.1 Definition of decay chain	2
2.2 Invariant mass end-points	3
3. Geometric interpretation	5
4. Additional kinematic constraints	7
4.1 Global end-point constraints	7
4.2 Conditional end-point constraints with two-dimensional correlations	8
4.3 Conditional end-point constraints with three-dimensional correlations	12
5. Mass reconstruction	15
6. Detector-level study	17
6.1 Introduction	17
6.2 Event simulation, selection and reconstruction	17
6.3 Global end-point analysis	18
6.4 Conditional end-point analysis	21
7. Conclusions	26

1. Introduction

Measurement of SUSY particle (‘sparticle’) masses in R-parity conserving SUSY events at hadron colliders such as the LHC is complicated by the pair production of invisible Lightest Supersymmetric Particles (LSPs), one of which terminates each SUSY particle decay chain. The presence of these LSPs prevents direct measurement of the masses of the sparticles participating in the decay chains via peaks in the invariant mass distributions of the observable SUSY decay products.

Several approaches to resolving this problem have been documented. These approaches may be grouped into three general categories. The first category consists of techniques which use the measurement of kinematic end-points in distributions of the invariant masses of combinations of visible SUSY decay products (jets, leptons etc.) from a single decay chain in each event. Given a long decay chain sufficient constraints may be obtained to solve for the individual masses [1, 2, 3, 4]. The second category consists of techniques which use the measurement of kinematic end-points in distributions of observables constructed from

the transverse momenta of SUSY decay products from two identical decay chains appearing in each event [5, 6, 7, 8]. These techniques can provide constraints on combinations of sparticle masses from very short (one-step) chains and can in principle lead to constraints on individual masses [7, 8, 9, 10, 11]. The third category consists of hybrid methods which seek to use optimally both transverse momentum and invariant mass constraints from a subset of events in which the same long decay chain appears in both ‘legs’ of each event (e.g. [12, 13]). Such techniques can offer an improvement on the mass constraints obtained by other techniques, but may require significant integrated luminosity to generate a sufficiently large sample of the specific events of interest.

This paper shall focus on the first category of mass measurement techniques – that involving the use of kinematic end-point constraints. The goal of the paper is to re-examine the constraints which may be obtained from kinematic end-points in the three-step sequential two-body decay chains most usually studied, with a focus on correlations between invariant mass observables. This will lead to a simplification of the technique and an improvement in the possible mass measurement precision. Similar techniques have been studied recently for the different case of events in which SUSY higgs particles decay symmetrically via two two-step sequential two-body decays [14, 15]. Correlations between invariant masses were also exploited in Ref. [12].

Section 2 commences with a review of the conventional end-point technique, while Section 3 re-interprets the technique from a geometric perspective. Section 4 examines the additional constraints which can be obtained by making use of correlations between invariant mass observables while Section 5 examines how these constraints may be used in principle to determine individual sparticle masses. Section 6 presents a case study in which the new techniques are used to measure sparticle masses for the SPS1a benchmark model with fast detector simulation. Section 7 concludes and outlines some possible directions for future work.

2. Kinematic constraints from three-step sequential two-body decay chains

2.1 Definition of decay chain

In many regions of SUSY parameter space the sparticle mass hierarchy is such that heavy strongly interacting sparticles produced in the initial proton-proton interaction can decay via a 3-step sequential two-body decay chain of the form:

$$\delta \rightarrow \gamma c \rightarrow \beta bc \rightarrow \alpha abc, \quad (2.1)$$

where Greek letters denote SUSY states, Roman letters denote visible SM decay products and α is the LSP. The canonical example of such a decay chain is the decay

$$\tilde{q}_L \rightarrow \tilde{\chi}_2^0 q \rightarrow \tilde{l}_R l_n q \rightarrow \tilde{\chi}_1^0 l_f l_n q, \quad (2.2)$$

where a left-squark decays via a chain consisting of the next-to-lightest neutralino, a right-slepton and a lightest neutralino (LSP), in the process emitting a quark (q) and two opposite-sign same-flavour leptons (l_n, l_f). The notation $l_n(l_f)$ is conventionally used

to denote the lepton emitted nearest to (furthest from) the quark in the decay chain. In practice l_n is indistinguishable from l_f which leads to ambiguities in the mass constraints obtained from this technique.

In this paper we shall illustrate mass measurement techniques at both parton and detector-level using the SPS1a benchmark SUSY model [16, 17]. The relevant mean sparticle masses for this model are $m_{\tilde{\chi}_1^0} = 96.05$ GeV, $m_{\tilde{l}_R} = 142.97$ GeV, $m_{\tilde{\chi}_2^0} = 176.82$ GeV and $491.9 \text{ GeV} < m_{\tilde{q}_L} < 543.0 \text{ GeV}$. In the \tilde{q}_L case we assume dominant light squark production and a common light squark mass of 540 GeV when constructing kinematic bounds. The limited validity of this simplifying assumption, together with the non-zero widths of the squarks (especially) causes some parton-level distributions to ‘leak’ beyond the expected bounds (see e.g. Figure 2 below). For this study **HERWIG 6.4** [18, 19] was used to generate 300k (100 fb^{-1}) parton-level SUSY events filtered to require at least two final state leptons in each event.

A note on notation In this paper we shall frequently refer both to global bounds on invariant mass distributions (‘global end-points’) and to bounds obtained from subsets of events satisfying certain selection criteria imposed on other invariant mass quantities (‘conditional end-points’). In common with previous studies we shall refer to the former with quantities with a single superscript ‘max’ or ‘min’. We shall refer to the latter with quantities with a superscript ‘max(m)’ where m represents the invariant mass upon which the selection criteria are imposed.

2.2 Invariant mass end-points

The end-point technique starts by constraining combinations of masses of sparticles appearing in the decay chain given by Eqn. (2.2) by using kinematic bounds (‘end-points’) in the distributions of the invariant masses of combinations of q , l_n and l_f . Maxima in the distributions of two-body invariant masses m_{ij} are obtained when visible particles i and j are emitted in opposite directions in the rest frame of the $\tilde{\chi}_2^0$ sparticle in each chain. Because each decay is two-body the momenta of i and j are fixed in the rest frames of their respective parents. Consequently there is a one-to-one mapping between the opening angles of the i and j in the rest frame of the $\tilde{\chi}_2^0$ and m_{ij} . Setting this angle to its maximum value of π radians therefore allows the position of the kinematic end-points to be determined analytically. The formulae are (see e.g. Ref. [1]):

$$(m_{ll}^{\max})^2 = \frac{(m_{\tilde{\chi}_2^0}^2 - m_{\tilde{l}_R}^2)(m_{\tilde{l}_R}^2 - m_{\tilde{\chi}_1^0}^2)}{m_{\tilde{l}_R}^2}, \quad (2.3)$$

$$(m_{ql_n}^{\max})^2 = \frac{(m_{\tilde{q}_L}^2 - m_{\tilde{\chi}_2^0}^2)(m_{\tilde{\chi}_2^0}^2 - m_{\tilde{l}_R}^2)}{m_{\tilde{\chi}_2^0}^2}, \quad (2.4)$$

$$(m_{ql_f}^{\max})^2 = \frac{(m_{\tilde{q}_L}^2 - m_{\tilde{\chi}_2^0}^2)(m_{\tilde{l}_R}^2 - m_{\tilde{\chi}_1^0}^2)}{m_{\tilde{l}_R}^2}. \quad (2.5)$$

For the following discussion it will also be useful to define a quantity $m_{qlf}^{\max(0)}$ which measures the maximum value of m_{qlf} when the two leptons are co-linear and hence $m_{ll} = 0$:

$$(m_{qlf}^{\max(0)})^2 = \frac{(m_{\tilde{q}_L}^2 - m_{\tilde{\chi}_2^0}^2)(m_{\tilde{l}_R}^2 - m_{\tilde{\chi}_1^0}^2)}{m_{\tilde{\chi}_2^0}^2}. \quad (2.6)$$

The ambiguity of assigning observed lepton momenta to l_n and l_f conventionally prevents direct measurement of m_{qln}^{\max} and m_{qlf}^{\max} . Instead, for each event the two possible lepton+quark(jet) invariant masses are ordered to generate $m_{ql(\text{hi})}^{\max}$ and $m_{ql(\text{lo})}^{\max}$ with analytical end-point positions at [2] (following Ref. [3]):

$$(m_{ql(\text{lo})}^{\max}, m_{ql(\text{hi})}^{\max}) = \left\{ \begin{array}{ll} (m_{qln}^{\max}, m_{qlf}^{\max}) & \text{for } 2m_{\tilde{l}_R}^2 > m_{\tilde{\chi}_1^0}^2 + m_{\tilde{\chi}_2^0}^2 > 2m_{\tilde{\chi}_1^0}m_{\tilde{\chi}_2^0} \\ (m_{ql(\text{eq})}^{\max}, m_{qlf}^{\max}) & \text{for } m_{\tilde{\chi}_1^0}^2 + m_{\tilde{\chi}_2^0}^2 > 2m_{\tilde{l}_R}^2 > 2m_{\tilde{\chi}_1^0}m_{\tilde{\chi}_2^0} \\ (m_{ql(\text{eq})}^{\max}, m_{qln}^{\max}) & \text{for } m_{\tilde{\chi}_1^0}^2 + m_{\tilde{\chi}_2^0}^2 > 2m_{\tilde{\chi}_1^0}m_{\tilde{\chi}_2^0} > 2m_{\tilde{l}_R}^2 \end{array} \right. \quad (2.7)$$

where

$$(m_{ql(\text{eq})}^{\max})^2 = \frac{(m_{\tilde{q}_L}^2 - m_{\tilde{\chi}_2^0}^2)(m_{\tilde{l}_R}^2 - m_{\tilde{\chi}_1^0}^2)}{(2m_{\tilde{l}_R}^2 - m_{\tilde{\chi}_1^0}^2)}. \quad (2.8)$$

The bound provided by $m_{ql(\text{eq})}^{\max}$ arises from kinematic configurations in which m_{ql} is maximised for $m_{qln} = m_{qlf} \equiv m_{ql(\text{eq})}$. Case A1 holds for the SPS1a model considered throughout this paper.

In addition to the two-body invariant mass end-points three-body end-points may be observed using m_{qll} . The analytical formula for the maximum value of the distribution of m_{qll} is complicated by the fact that it may be generated by any one of four kinematic configurations, depending on the sparticle mass hierarchy. These configurations are those in which two of q , l_n and l_f lie co-linear in the $\tilde{\chi}_2^0$ rest frame and one contra-linear (three configurations) or their net momentum in the \tilde{q}_L rest-frame is zero (one configuration). Taking this ambiguity into account the maximum value of the m_{qll} distribution is found to lie at [2] (following Ref. [3]):

$$(m_{qll}^{\max})^2 = \left\{ \begin{array}{ll} \frac{(m_{\tilde{q}_L}^2 - m_{\tilde{\chi}_2^0}^2)(m_{\tilde{\chi}_2^0}^2 - m_{\tilde{\chi}_1^0}^2)}{m_{\tilde{\chi}_2^0}^2} & \text{for } \frac{m_{\tilde{q}_L}}{m_{\tilde{\chi}_2^0}} > \frac{m_{\tilde{\chi}_2^0}}{m_{\tilde{l}_R}} \frac{m_{\tilde{l}_R}}{m_{\tilde{\chi}_1^0}} \\ \frac{(m_{\tilde{q}_L}^2 m_{\tilde{l}_R}^2 - m_{\tilde{\chi}_2^0}^2 m_{\tilde{\chi}_1^0}^2)(m_{\tilde{\chi}_2^0}^2 - m_{\tilde{l}_R}^2)}{m_{\tilde{\chi}_2^0}^2 m_{\tilde{l}_R}^2} & \text{for } \frac{m_{\tilde{\chi}_2^0}}{m_{\tilde{l}_R}} > \frac{m_{\tilde{l}_R}}{m_{\tilde{\chi}_1^0}} \frac{m_{\tilde{q}_L}}{m_{\tilde{\chi}_2^0}} \\ \frac{(m_{\tilde{q}_L}^2 - m_{\tilde{l}_R}^2)(m_{\tilde{l}_R}^2 - m_{\tilde{\chi}_1^0}^2)}{m_{\tilde{l}_R}^2} & \text{for } \frac{m_{\tilde{l}_R}}{m_{\tilde{\chi}_1^0}} > \frac{m_{\tilde{q}_L}}{m_{\tilde{\chi}_2^0}} \frac{m_{\tilde{\chi}_2^0}}{m_{\tilde{l}_R}} \\ (m_{\tilde{q}_L} - m_{\tilde{\chi}_1^0})^2 & \text{otherwise} \end{array} \right. \quad (2.9)$$

The first three cases above (B1–B3) occur if one of the three co-linear configurations provides the maximum m_{qll} value, with cases B1, B2 and B3 corresponding respectively to configurations with $\{m_{qlf} = m_{qlf}^{\max(0)}, m_{ll} = 0, m_{qln} = m_{qln}^{\max}\}$, $\{m_{qlf} = 0, m_{ll} = m_{ll}^{\max}, m_{qln} =$

$m_{qln}^{\max}\}$ and $\{m_{qlf} = m_{qlf}^{\max}, m_{ll} = m_{ll}^{\max}, m_{qln} = 0\}$. The fourth case (B4) occurs if the zero momentum configuration is allowed kinematically. Case B1 holds for the SPS1a model considered throughout this paper.

The m_{qll} distribution also possesses a non-zero minimum when $m_{ll} > 0$. Conventionally a cut requiring $m_{ll} > m_{ll}^{\max}/\sqrt{2}$ is applied, leading to a threshold in the m_{qll} distribution at m_{qll}^{\min} given by¹ :

$$\begin{aligned} (m_{qll}^{\min})^2 = \frac{1}{4m_{\tilde{l}_R}^2 m_{\tilde{\chi}_2^0}^2} & \left[2m_{\tilde{l}_R}^2 (m_{\tilde{q}_L}^2 - m_{\tilde{\chi}_2^0}^2) (m_{\tilde{\chi}_2^0}^2 - m_{\tilde{\chi}_1^0}^2) \right. \\ & + (m_{\tilde{q}_L}^2 + m_{\tilde{\chi}_2^0}^2) (m_{\tilde{\chi}_2^0}^2 - m_{\tilde{l}_R}^2) (m_{\tilde{l}_R}^2 - m_{\tilde{\chi}_1^0}^2) \\ & \left. - (m_{\tilde{q}_L}^2 - m_{\tilde{\chi}_2^0}^2) \sqrt{(m_{\tilde{\chi}_2^0}^2 + m_{\tilde{l}_R}^2)^2 (m_{\tilde{l}_R}^2 + m_{\tilde{\chi}_1^0}^2)^2 - 16m_{\tilde{\chi}_2^0}^2 m_{\tilde{l}_R}^4 m_{\tilde{\chi}_1^0}^2} \right]. \end{aligned} \quad (2.10)$$

Together these five mass constraints may be solved numerically [1, 2] or analytically [4] to determine the four individual sparticle masses $m_{\tilde{q}_L}$, $m_{\tilde{\chi}_2^0}$, $m_{\tilde{l}_R}$ and $m_{\tilde{\chi}_1^0}$. In either case the ambiguities in the interpretation of $m_{ql(hi)}^{\max}$, $m_{ql(lo)}^{\max}$ and m_{qll}^{\max} can lead to multiple solutions and hence ambiguity in constraints on the underlying SUSY model. This is discussed extensively in e.g. Ref. [4].

3. Geometric interpretation

The conventional approach to the derivation of kinematic end-point constraints illustrated above focuses on physical configurations of particle momenta which maximise or minimise invariant masses. The constraints are thus generated when the momentum vectors of visible particles are correlated in a particular manner, for instance parallel or anti-parallel. Let us now generalise this argument to reinterpret these correlations in a geometric context. Our aim will be to use these momentum correlations to identify correlations between the invariant masses constructed from the momenta. For convenience we shall work in the rest frame of the $\tilde{\chi}_2^0$ in the following discussion, however the calculated invariant masses are clearly equal to those measured in the laboratory frame.

Our starting point is the observation that extremal values of m_{qll} are obtained when the momenta of q , l_n and l_f lie in the same plane in the rest frame of the $\tilde{\chi}_2^0$. Furthermore the extremal values of m_{ll} , m_{qln} and m_{qlf} can trivially also be obtained when this is the case. Neglecting the masses of q , l_n and l_f we can write the three invariant mass combinations as:

$$m_{ll} = 2p_{l_n}p_{l_f}(1 - \cos\theta_{ll}), \quad (3.1)$$

$$m_{qln} = 2p_{q}p_{l_n}(1 - \cos\theta_{qln}), \quad (3.2)$$

$$m_{qlf} = 2p_{q}p_{l_f}(1 - \cos\theta_{qlf}), \quad (3.3)$$

¹The value of m_{qll}^{\min} is dependent on the condition imposed upon m_{ll} and therefore should strictly be identified in this paper as $m_{qll}^{\min(m_{ll})}$, in light of the discussion in Section 2.1. We choose to retain the notation m_{qll}^{\min} for consistency with earlier work however.

where p_i denotes the magnitude of the three-momentum of particle i and θ_{ij} denotes the opening angle between the three-momenta of particles i and j . When q , l_n and l_f all lie in one plane we have the further relation:

$$\theta_{ll} + \theta_{ql_n} + \theta_{ql_f} = 2\pi. \quad (3.4)$$

Now in the rest frame of the $\tilde{\chi}_2^0$ the momentum magnitude p_{l_n} is determined from simple two-body kinematics to be the fixed quantity:

$$p_{l_n} = \frac{m_{\tilde{\chi}_2^0}^2 - m_{\tilde{l}_R}^2}{2m_{\tilde{\chi}_2^0}}. \quad (3.5)$$

The momentum magnitude p_q is also fixed in this frame to be:

$$p_q = \frac{m_{\tilde{q}_L}^2 - m_{\tilde{\chi}_2^0}^2}{2m_{\tilde{\chi}_2^0}}. \quad (3.6)$$

The magnitude of the momentum of l_f , p_{l_f} , is however not a constant in this frame – it is related to the fixed momentum magnitude p'_{l_f} measured in the rest frame of the \tilde{l}_R by a Lorentz transformation dependent on θ_{ll} :

$$\begin{aligned} p'_{l_f} &\equiv \frac{m_{\tilde{l}_R}^2 - m_{\tilde{\chi}_1^0}^2}{2m_{\tilde{l}_R}} \\ &= \gamma p_{l_f} (1 + \beta \cos \theta_{ll}), \end{aligned} \quad (3.7)$$

where the boost factor β is given by:

$$\beta = \frac{m_{\tilde{\chi}_2^0}^2 - m_{\tilde{l}_R}^2}{m_{\tilde{\chi}_2^0}^2 + m_{\tilde{l}_R}^2}, \quad (3.8)$$

and $\gamma = (1 - \beta^2)^{-1/2}$.

It is convenient now to define three dimensionless mass coordinates x , y and z :

$$x = \frac{m_{ql_n}}{\sqrt{p_q p_{l_n}}}, \quad (3.9)$$

$$y = \frac{m_{ql_f}}{\sqrt{p_q p'_{l_f}}}, \quad (3.10)$$

$$z = \frac{m_{ll}}{\sqrt{p_{l_n} p'_{l_f}}}, \quad (3.11)$$

together with a dimensionless mass ratio $r \equiv m_{\tilde{l}_R}/m_{\tilde{\chi}_2^0}$. We can now use Eqns. (3.1)–(3.3) to express Eqn. (3.4) purely in terms of invariant masses m_{ij} and momenta and then substitute from Eqns. (3.9)–(3.11) to obtain a single relation between x , y and z :

$$\left(x^2 \left(r + \frac{1}{4} (1 - r^2) z^2 \right) - y^2 - z^2 \right)^2 + (x^2 - 4)y^2 z^2 = 0. \quad (3.12)$$

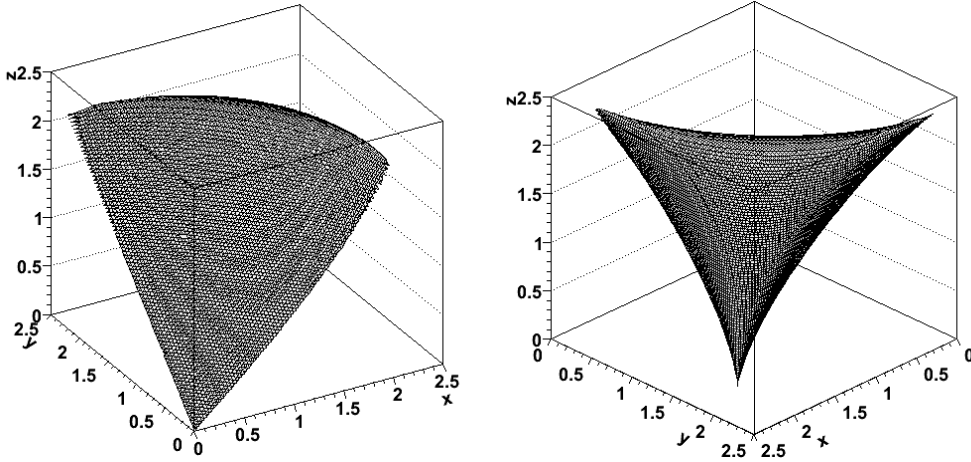


Figure 1: Σ_{qll} surface for the SPS1a benchmark SUSY model plotted in $x - y - z$ space and viewed from two different perspectives.

Eqn. (3.12) defines a surface Σ_{qll} in the 3-dimensional $x - y - z$ space. This surface bounds the region within which all decay chains of the type Eqn. (2.2) must lie: events in which the visible decay products are coplanar lie on the surface, while acoplanar events lie within the volume. The surface is plotted in Figure 1 for the SPS1a benchmark model. A key feature to note is that Σ_{qll} intersects the planes with x , y or z zero along lines, since when any one m_{ij} value is zero, particles i and j must be co-linear and hence m_{jk} must be uniquely determined by m_{ki} (and vice versa). Note in addition that if Σ_{qll} were plotted in $m_{qln} - m_{qlf} - m_{ll}$ space rather than in $x - y - z$ space the radial distance from the origin of a point on Σ_{qll} would give m_{qll} , and hence in these coordinates m_{qll}^{\max} represents the greatest radial distance of a point on Σ_{qll} from the origin. Eqn. (3.12) shall prove useful for deriving some of the kinematic bounds in two- and three-dimensions discussed below however it is potentially also useful in its own right – for instance for selecting events with the decay chain Eqn. 2.2 and associating decay products with specific steps in that decay chain once the masses of the sparticles are known.

4. Additional kinematic constraints

4.1 Global end-point constraints

Constraints on the masses of the sparticles participating in the decay chain listed in Eqn. (2.2) can be obtained by measuring the surface Σ_{qll} defined by Eqn. (3.12). The techniques described in Section 2.2 rely on integrating out all but one invariant mass observable and then measuring the global end-point in the resulting mass distribution. It should be clear from the discussion of Section 3 however that there is potentially much more information contained in Eqn. (3.12) than can be exploited with this relatively simple technique. In particular the shape of this surface can be measured in more detail by exploiting correlations between invariant mass observables. Such correlations are partially exploited by the definition of the m_{qll}^{\min} end-point in Eqn. (2.10), in which the integration

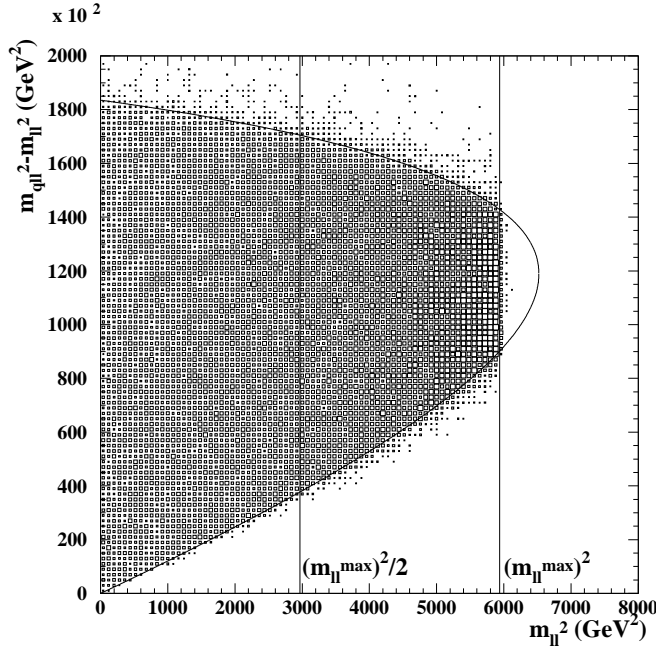


Figure 2: Parton-level two-dimensional invariant mass-squared distribution for decay chain Eqn. (2.2) for the SPS1a benchmark model showing $m_{qll}^2 - m_{ll}^2$ plotted against m_{ll}^2 . See text for explanation of bounds.

takes place only over a limited range in m_{ll} , however the possibilities presented by this technique are more numerous, as shall be illustrated in the following discussion.

4.2 Conditional end-point constraints with two-dimensional correlations

The first class of additional constraints can be obtained by integrating over only one, rather than two, of the three degrees-of-freedom used to define the surface Σ_{qll} in Eqn. (3.12). The most familiar example of such a technique is that used to obtain the m_{qll}^{\min} end-point discussed above. The correlation between m_{qll} and m_{ll} can be observed by plotting $m_{qll}^2 - m_{ll}^2$ against m_{ll}^2 , shown at parton-level in Figure 2 for the SPS1a benchmark model. The vertical kinematic bound in this figure is provided by m_{ll}^{\max} (right-hand vertical line), while the minimum of the one-dimensional distribution obtained by integrating along the m_{ll}^2 axis to the right of the left-hand vertical line measures $(m_{qll}^{\min})^2 - (m_{ll}^{\max})^2/2$.

The curved bounds in Figure 2 may be obtained from the general formula (see e.g. Ref. [20]) for the end-points in the invariant mass distribution of two heavy visible decay products a and b of a two-step sequential two-body decay chain $\gamma \rightarrow \beta b \rightarrow \alpha ab$:

$$(m_{ab}^{\text{bound}(m_a, m_b)})^2 = m_a^2 + m_b^2 + \frac{1}{2m_\beta^2} \left[(m_\beta^2 - m_\alpha^2 + m_a^2)(m_\gamma^2 - m_\beta^2 - m_b^2) \right. \\ \left. \pm \sqrt{\lambda(m_\beta, m_\alpha, m_a)\lambda(m_\gamma, m_\beta, m_b)} \right], \quad (4.1)$$

where

$$\lambda(m_i, m_j, m_k) \equiv (m_i^2 - m_j^2 + m_k^2)^2 - 4m_i^2 m_k^2. \quad (4.2)$$

When $a \equiv ll$ and $b \equiv q$ and $m_b = 0$ this equation may be simplified to give:

$$(m_{qll}^{\text{bound}(m_{ll})})^2 = m_{ll}^2 + \frac{(m_{\tilde{q}L}^2 - m_{\tilde{\chi}_2^0}^2)}{2m_{\tilde{\chi}_2^0}^2} \left(m_{\tilde{\chi}_2^0}^2 - m_{\tilde{\chi}_1^0}^2 + m_{ll}^2 \pm \sqrt{\lambda(m_{\tilde{\chi}_2^0}, m_{\tilde{\chi}_1^0}, m_{ll})} \right), \quad (4.3)$$

where the positive root corresponds to the usual expression for the ‘ m_{Xq}^{\max} ’ end-point with $X \equiv ll$ [1]. The two roots of this equation correspond to the upper and lower curved bounds in Figure 2. Setting $m_a = 0$ with $a \equiv l_f$ and $b \equiv ql_n$ in Eqn. (4.1) also allows the equivalent bounds in the $m_{qlf}^2 - m_{qln}^2$ versus m_{qln}^2 distribution to be obtained (not shown).

Plots similar to Figure 2 can also be constructed from the distributions of $m_{qlf}^2 - m_{qln}^2$ as a function of m_{qln}^2 and $m_{qlf}^2 - m_{qlf}^2$ as a function of m_{qlf}^2 . In the latter case however the kinematic bounds are particularly difficult to describe analytically. An alternative means of illustrating two-dimensional correlations in which the kinematic bounds may be described more easily is provided by the distributions of m_{ij}^2 as functions of m_{jk}^2 where i, j and k are drawn from q, l_n and l_f . The three possible distributions are shown in Figure 3 at parton-level for the SPS1a model. Squared masses are plotted in this and subsequent figures in this section (as in Figure 2) as this generates kinematic bounds which take on particularly simple forms.

In Figure 3 the bounds on m_{qlf}^2 , m_{qln}^2 and m_{ll}^2 obtained from the conventional ‘global end-point’ analysis together with $(m_{qlf}^{\max(0)})^2$ are illustrated by vertical and horizontal lines (labelled). In the top-right and bottom figures the upper bounds on m_{qlf}^2 lie respectively at:

$$(m_{qlf}^{\max(m_{ll})})^2 = (m_{qlf}^{\max(0)})^2 + \left[(m_{qlf}^{\max})^2 - (m_{qlf}^{\max(0)})^2 \right] \left(\frac{m_{ll}}{m_{ll}^{\max}} \right)^2, \quad (4.4)$$

and

$$(m_{qlf}^{\max(m_{qln})})^2 = (m_{qlf}^{\max})^2 - \left[(m_{qlf}^{\max})^2 - (m_{qlf}^{\max(0)})^2 \right] \left(\frac{m_{qln}}{m_{qln}^{\max}} \right)^2. \quad (4.5)$$

Of course in practice we can not distinguish m_{qlf} from m_{qln} on an event-by-event basis. For this reason we plot in Figure 4 the equivalent distributions to Figure 3 for $m_{ql(\text{lo})}^2$ and $m_{ql(\text{hi})}^2$ rather than m_{qln}^2 and m_{qlf}^2 . As expected the distributions resemble combinations of the m_{qln}^2 and m_{qlf}^2 distributions, with an additional bound where $m_{qln} = m_{qlf} = m_{ql(\text{eq})}$. This bound is trivial in Figure 4(bottom) while in the top-left and top-right figures the equation of the bound can be obtained by using Eqn. (3.12) and Eqns. (3.9)–(3.11) and solving the resulting quadratic equation for $m_{ql(\text{eq})}^2$ as a function of m_{ll}^2 :

$$(m_{ll}^2 + A^2)m_{ql(\text{eq})}^4 - 2m_{ll}^2 p_q (2p_{l_n} + A)m_{ql(\text{eq})}^2 + m_{ll}^4 p_q^2 = 0, \quad (4.6)$$

where

$$A \equiv r p'_{l_f} - p_{l_n} + (1 - r^2) \frac{m_{ll}^2}{4p_{l_n}}. \quad (4.7)$$

The two roots of this equation give the upper and lower curved bounds in these figures.

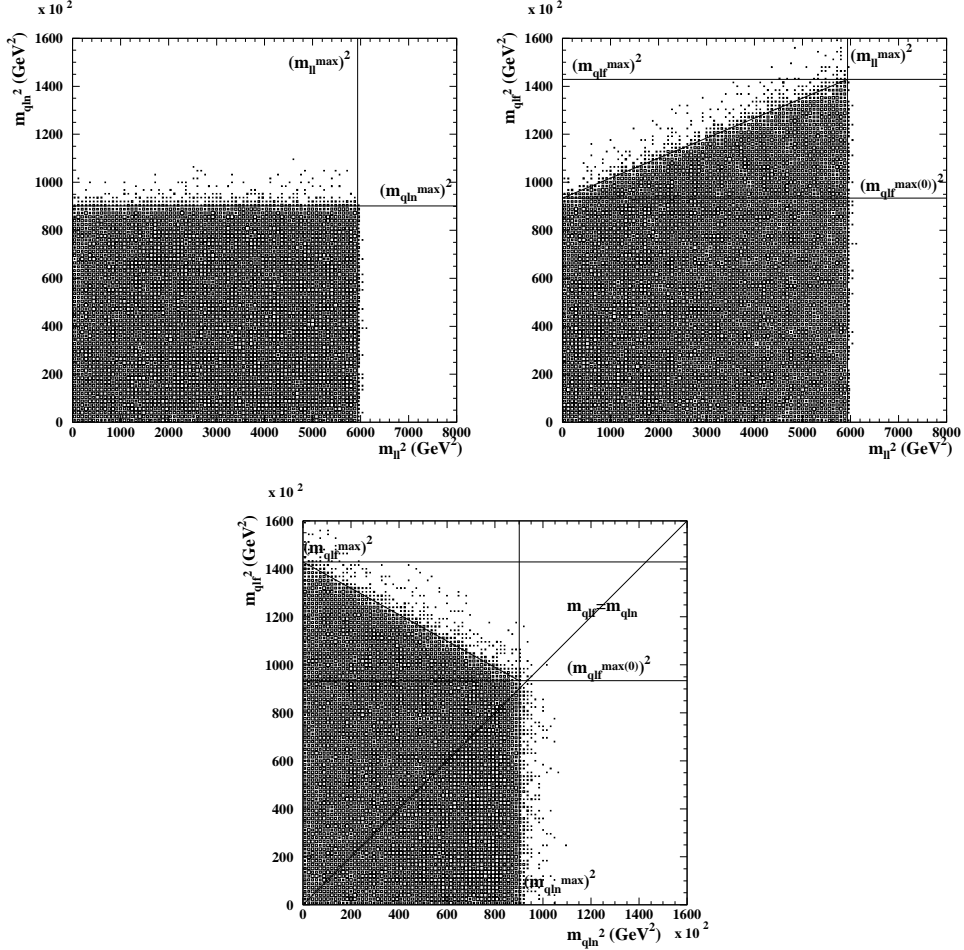


Figure 3: Parton-level two-dimensional invariant mass-squared distributions for decay chain Eqn. (2.2) for the SPS1a benchmark model. The top-left figure shows the distribution of m_{qln}^2 as a function of m_{ll}^2 , the top-right figure the distribution of m_{qlf}^2 as a function of m_{ll}^2 and the bottom figure the distribution of m_{qlf}^2 as a function of m_{qln}^2 . See text for explanation of bounds.

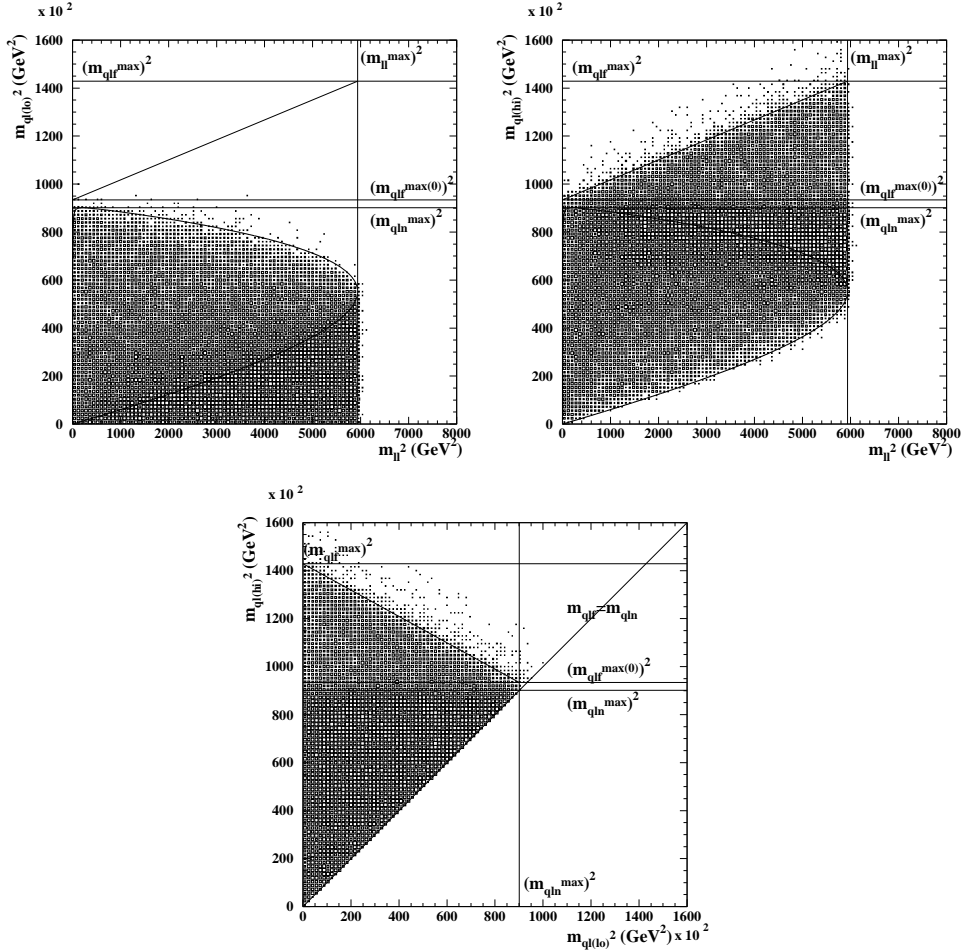


Figure 4: Observable two-dimensional parton-level invariant mass-squared distributions for decay chain Eqn. (2.2) for the SPS1a benchmark model. The top-left figure shows the distribution of $m_{ql(0)}^2$ as a function of m_{ll}^2 , the top-right figure the distribution of $m_{ql(hi)}^2$ as a function of m_{ll}^2 and the bottom figure the distribution of $m_{ql(hi)}^2$ as a function of $m_{ql(0)}^2$. See text for explanation of bounds.

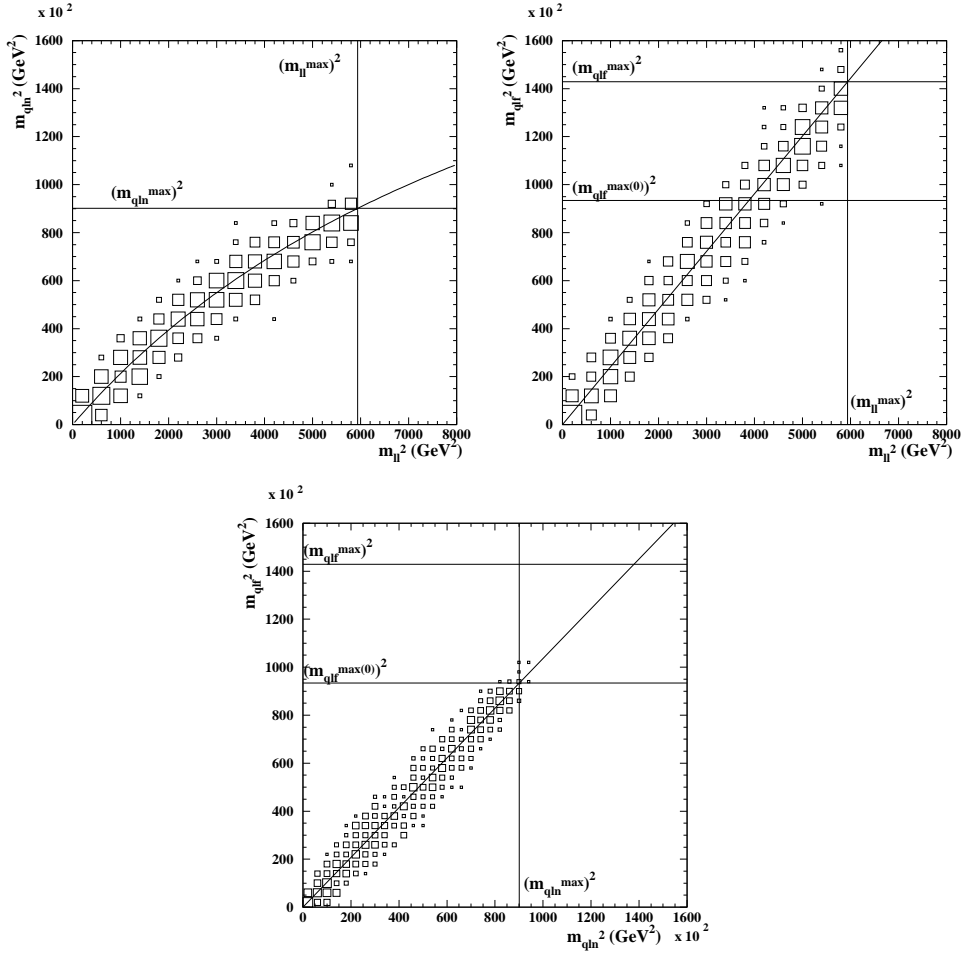


Figure 5: Two-dimensional distributions of two-particle invariant masses for the SPS1a model, with the third invariant mass required to be less than 50 GeV (top figures) or less than 10 GeV (bottom figure). The top-left figure shows m_{qln}^2 versus m_{ll}^2 , the top-right figure m_{qlf}^2 versus m_{ll}^2 , and the bottom figure m_{qln}^2 versus m_{qlf}^2 . See text for explanation of bounds and loci.

4.3 Conditional end-point constraints with three-dimensional correlations

A second class of constraints can be obtained from Eqn (3.12) by measuring invariant mass correlations without integration over additional mass distributions. In principle this could be used to measure Σ_{qll} directly. Here we provide one example of such a technique in which we study the form of the one-dimensional lines where Σ_{qll} intersects the planes with respectively x , y and z (or equivalently m_{qln} , m_{qlf} and m_{ll}) equal to zero. The resulting mass-squared distributions are analogous to those shown in Figures 3 and 4 but with the additional requirement that the third mass(-squared) value not plotted in each figure is small.

We proceed by requiring m_{qln} , m_{qlf} or m_{ll} to be less than some value (here set to 50 GeV for m_{ql} quantities and 10 GeV for m_{ll})² sufficiently large to provide useful statistics but

²With these selection requirements the mean quark-lepton(lepton-lepton) separation is $\Delta R = 0.6(0.2)$.

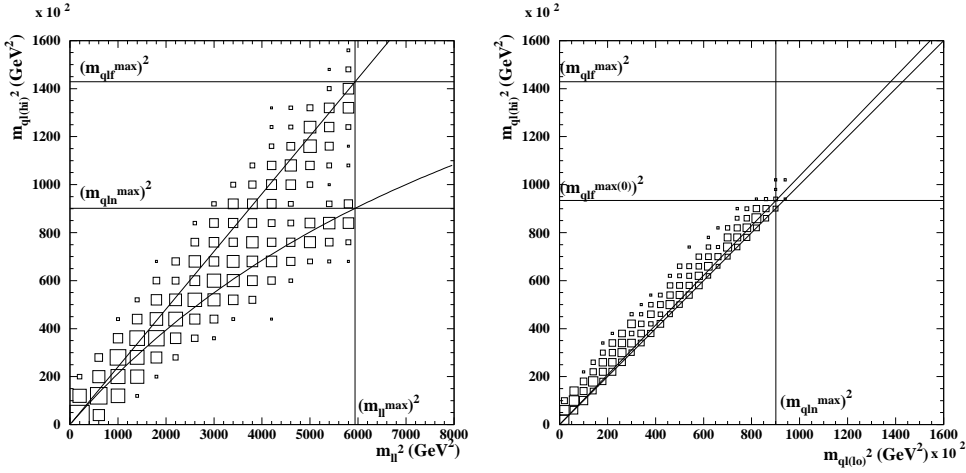


Figure 6: Observable distributions constructed from the quantities plotted in Figure 5 for the SPS1a benchmark model. The lower of the two diagonal lines in the right-hand figure represents the trivial bound where $m_{ql(hi)} = m_{ql(lo)}$. The remaining bounds and loci are as for Figure 5 (see text).

sufficiently small to approximately maintain the one-dimensional form of the intersection. We then plot the two-dimensional distribution of the two unconstrained squared masses in each case. These distributions can be seen in Figure 5. In the top-left and top-right figures the vertical lines represent the bound from $(m_{ll}^{\max})^2$, while the horizontal lines represent the bounds from $(m_{ql_n}^{\max})^2$, $(m_{ql_f}^{\max})^2$ and $(m_{ql_f}^{\max(0)})^2$. In the bottom figure the vertical and horizontal lines represent the bounds from $(m_{ql_n}^{\max})^2$ and $(m_{ql_f}^{\max(0)})^2$ respectively. The loci of the distributions in the figures are given in terms of dimensionless mass coordinates by:

$$x^2(y=0) = \frac{z^2}{r + \frac{1}{4}(1-r^2)z^2}, \quad (4.8)$$

$$y^2(x=0) = z^2, \quad (4.9)$$

$$y^2(z=0) = x^2r, \quad (4.10)$$

which gives the following relations:

$$m_{ql_n}^2 = m_{ll}^2 \left(\frac{m_{\tilde{q}_L}^2 - m_{\tilde{\chi}_2^0}^2}{m_{\tilde{l}_R}^2 - m_{\tilde{\chi}_1^0}^2 + m_{ll}^2} \right), \quad (4.11)$$

$$m_{ql_f}^2 = m_{ll}^2 \left(\frac{m_{\tilde{q}_L}^2 - m_{\tilde{\chi}_2^0}^2}{m_{\tilde{\chi}_2^0}^2 - m_{\tilde{l}_R}^2} \right), \quad (4.12)$$

$$m_{ql_f}^2 = m_{ql_n}^2 \left(\frac{m_{\tilde{l}_R}^2 - m_{\tilde{\chi}_1^0}^2}{m_{\tilde{\chi}_2^0}^2 - m_{\tilde{l}_R}^2} \right). \quad (4.13)$$

If these object separations were too small in practice to provide useful lepton reconstruction efficiency they could be increased at the expense of mass resolution (see text).

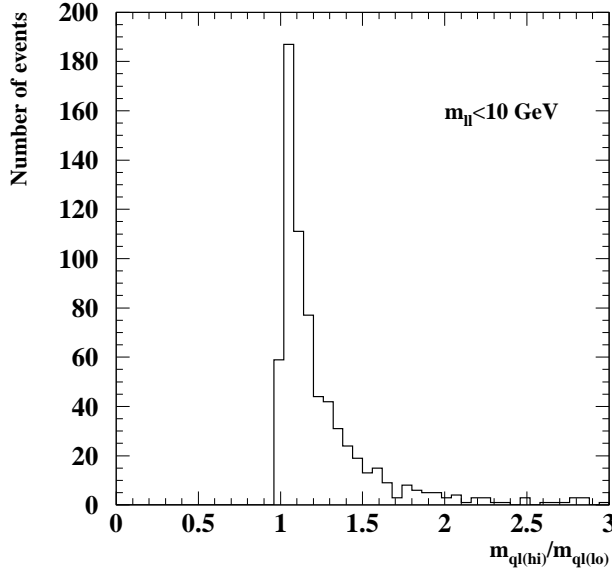


Figure 7: Distribution of the ratio $m_{ql(hi)}/m_{ql(lo)}$ for $m_{ll} < 10$ GeV for the SPS1a benchmark SUSY model. The distribution possesses a trivial bound at $m_{ql(hi)}/m_{ql(lo)} = 1$ while the prominent peak is indicative of sequential two-body lepton producing decays.

The distributions in Figure 5 are not observable directly due to the l_n/l_f ambiguity. Instead the three distributions of Figure 5 are replaced by two distributions (with $m_{ql(lo)}$ required to be small), plotted in Figure 6. If the loci in this figure can be identified in the presence of realistic detector-level smearing then they could be used to measure sparticle masses via Eqns. (4.11)–(4.13). In addition however Figure 6(right) can be used to determine whether the decay chain in selected events consists of two sequential two-body lepton-producing decays (as in Eqn. (2.2)) or a single three- (or more) body decay (e.g. $\tilde{\chi}_2^0 \rightarrow l^+ l^- \tilde{\chi}_1^0$). In the latter case m_{ll} can acquire a small value through one of the two leptons acquiring a very small momentum in the $\tilde{\chi}_2^0$ rest frame, while in the former case this can only occur due to event topology, i.e. due to the two leptons being emitted collinearly in this frame. This conclusion may also be reached by observing that Σ_{qll} defined in Eqn. (3.12) does not intersect any of the x , y or z coordinate axes and instead intersects the $x = 0$, $y = 0$ and $z = 0$ planes in one-dimensional lines generating the loci shown in Figure 5. The consequence of this observation is that in the three-body case $m_{ql(hi)}$ and $m_{ql(lo)}$ should be rather less correlated than in the sequential two-body case, where $m_{ql(hi)}$ is linearly related to $m_{ql(lo)}$ as shown in Figure 6(right). A convenient means of observing this correlation is to plot the one dimensional distribution of the ratio $m_{ql(hi)}/m_{ql(lo)}$ shown in Figure 7, where the presence of the prominent peak provides evidence for the presence of sequential two-body lepton producing decays. This provides a useful alternative to conventional techniques such as studying the shape of the m_{ll} distribution or measuring the ratio $m_{ql(hi)}^{\max}/m_{ql(lo)}^{\max}$ (which equals $\sqrt{2}$ for three-body lepton-producing decays [21]).

The kinematic bounds for three-body lepton-producing decay chains incorporating single two-body quark-producing decays are listed for completeness in Appendix A.

5. Mass reconstruction

Having identified some correlations between invariant mass observables we shall now discuss how they might be used in principle to constrain individual sparticle masses.

We start by observing that measurements of the global end-points together with measurements of the straight-line upper bounds in the two-dimensional distributions shown in Figure 4 can in principle give direct access to the four ‘core’ two-body observables m_{ll}^{\max} , $m_{ql_n}^{\max}$, $m_{ql_f}^{\max}$ and $m_{ql_f}^{\max(0)}$. In order to measure these quantities however we must first resolve or evade the ambiguities in the interpretation of the m_{ql} and m_{qll} end-points listed in Eqns. (2.7) and (2.9). This can be accomplished by examining the form of the kinematic bounds in Figures 3 and 4. The upper $m_{ql_n}^2$ bound (top-left panel of Figure 3) is constant as a function of m_{ll}^2 , while the equivalent $m_{ql_f}^2$ bound (top-right panel of Figure 3) is a linear function of m_{ll}^2 with non-zero gradient (in the absence of sparticle mass degeneracies). Consequently if the conditional upper bound on $m_{ql(\text{hi})}$ changes with m_{ll} then $m_{ql(\text{hi})}^{\max} = m_{ql_f}^{\max}$, corresponding to cases A1 and A2 in Eqn. (2.7). This is the situation for SPS1a. Conversely if the upper bound on $m_{ql(\text{hi})}$ remains constant with m_{ll} then $m_{ql(\text{hi})}^{\max} = m_{ql_n}^{\max}$, which corresponds to case A3 in Eqn. (2.7), and hence also $m_{ql(\text{lo})}^{\max} = m_{ql(\text{eq})}^{\max}$.

In order to discriminate between cases A1 and A2 we could in principle examine the behaviour of the conditional upper bound on $m_{ql(\text{lo})}$ as a function of m_{ll} . If the bound is constant in the vicinity of $m_{ql(\text{lo})}^{\max}$ then $m_{ql(\text{lo})}^{\max} = m_{ql_n}^{\max}$ (case A1, realised at SPS1a), while if it changes as a function of m_{ll} then $m_{ql(\text{lo})}^{\max} = m_{ql(\text{eq})}^{\max}$ (case A2). Equivalently, if the distribution of $m_{ql(\text{hi})}$ values as a function of $m_{ql(\text{lo})}$ (shown for squared masses in Figure 4(bottom)) is bounded in $m_{ql(\text{lo})}$ by a vertical line then $m_{ql(\text{lo})}^{\max} = m_{ql_n}^{\max}$ (case A1) but if it is bounded by a point then $m_{ql(\text{lo})}^{\max} = m_{ql(\text{eq})}^{\max}$ (case A2). Nevertheless the (squared mass) distributions shown in Figure 4 for SPS1a, for which $m_{ql_n}^{\max}$ is very close to $m_{ql(\text{eq})}^{\max}$, illustrate the difficulty of this strategy for resolving the $m_{ql(\text{lo})}^{\max}$ ambiguity. It is far from clear in these parton-level distributions whether these conditions are satisfied and at detector-level the difficulties will be still greater. In this case however we can potentially also make use of the fact that the upper bound on $m_{ql_n}^2$ shown in Figure 3(top-left) is also visible in the top-right and bottom panels of Figure 4 as a discontinuity in the $m_{ql(\text{hi})}^2$ distribution below its upper bound. Consequently observation of a ‘hidden’ bound in the $m_{ql(\text{hi})}$ distribution, with a position independent of any conditions imposed upon m_{ll} would enable $m_{ql_n}^{\max}$ to be measured directly, evading the A1/A2 ambiguity.

In cases A1 (e.g. SPS1a) or A2 the conditional upper bound on $m_{ql(\text{hi})}$ as a function of m_{ll} allows $m_{ql_f}^{\max}$ and $m_{ql_f}^{\max(0)}$ to be determined with Eqns. (4.4). Together with the measurement of $m_{ql_n}^{\max}$ discussed above and the measurement of the m_{ll}^{\max} end-point all four core two-body observables can hence be accessed. In case A3 it is the upper bound on m_{ql_f} which is hidden but nevertheless it may still be observable below the upper bound on $m_{ql(\text{hi})}$ provided here by the upper bound on m_{ql_n} . If this is the case then all four core two-body observables can again be determined. There are certainly special cases

where the sparticle mass values conspire to prevent ambiguity resolution on the basis of these arguments, however in those cases the use of multiple redundant measurements, for instance bounds on m_{qll} , should help to resolve these ambiguities (see e.g. Ref. [4]). The m_{ll} dependence of the conditional upper or lower bounds on $m_{ql(hi)}$ and $m_{ql(lo)}$ (shown for squared masses in Figure 4) could also be exploited.

An additional input to the mass reconstruction can be provided by the global upper bound on m_{qll} provided by m_{qll}^{\max} . This bound also suffers from ambiguities, as listed in Eqn. (2.9). Having resolved the ambiguities in m_{ql} however these ambiguities are considerably easier to address. The three cases corresponding to co-linear kinematic configurations (B1–B3) possess $(m_{qll}^{\max})^2$ values of respectively $(m_{ql_f}^{\max(0)})^2 + (m_{ql_n}^{\max})^2$, $(m_{ll}^{\max})^2 + (m_{ql_n}^{\max})^2$, and $(m_{ql_f}^{\max})^2 + (m_{ll}^{\max})^2$. Consequently the position of the value of m_{qll}^{\max} is already uniquely specified by independent measurements of the four core two-body observables. If $(m_{qll}^{\max})^2$ does not equal any of these three values within errors then case B4 is likely to provide the bound and hence an additional kinematic constraint. It should be noted that further mass constraints can in principle be obtained using Eqn. (2.9) by measuring the dependence of the conditional upper bound on m_{qll} as a function of m_{ll} together with the similar dependence of the conditional lower bound on m_{qll} , from which the global m_{qll}^{\min} end-point derives.

If we can unambiguously measure at least the four core two-body observables then we can obtain the individual sparticle masses analytically from:

$$m_{\tilde{\chi}_1^0} = \frac{m_{ll}^{\max} m_{ql_f}^{\max(0)}}{(m_{ql_f}^{\max})^2 - (m_{ql_f}^{\max(0)})^2} \sqrt{(m_{ql_n}^{\max})^2 - (m_{ql_f}^{\max})^2 + (m_{ql_f}^{\max(0)})^2}, \quad (5.1)$$

$$m_{\tilde{l}_R} = \frac{m_{ll}^{\max} m_{ql_n}^{\max} m_{ql_f}^{\max(0)}}{(m_{ql_f}^{\max})^2 - (m_{ql_f}^{\max(0)})^2}, \quad (5.2)$$

$$m_{\tilde{\chi}_2^0} = \frac{m_{ll}^{\max} m_{ql_n}^{\max} m_{ql_f}^{\max}}{(m_{ql_f}^{\max})^2 - (m_{ql_f}^{\max(0)})^2}, \quad (5.3)$$

$$m_{\tilde{q}_L} = \frac{m_{ql_n}^{\max} m_{ql_f}^{\max}}{(m_{ql_f}^{\max})^2 - (m_{ql_f}^{\max(0)})^2} \sqrt{(m_{ll}^{\max})^2 + (m_{ql_f}^{\max})^2 - (m_{ql_f}^{\max(0)})^2}. \quad (5.4)$$

Additional constraints, for instance provided by m_{qll}^{\max} , m_{qll}^{\min} or measurements of the conditional upper or lower bounds on $m_{ql(hi)}$ and $m_{ql(lo)}$ can be included in several equivalent ways. One approach involves replacing the analytical formulae of Eqns. (5.1)–(5.4) with a numerical fit to the sparticle masses incorporating all constraints. This approach is discussed further in Section 6. An alternative procedure involves re-casting the constraint equations in terms of the four core two-body observables and using a numerical fit to determine these quantities, retaining the analytical formulae for determining the sparticle masses in a second step. In this approach Eqns. (4.3) and (4.6) can be re-cast in terms of $m_{ql_n}^{\max}$, $m_{ql_f}^{\max}$, $m_{ql_f}^{\max(0)}$ and m_{ll}^{\max} with Eqns. (5.1)–(5.4) together with the equations relating

these quantities to the momenta of the jets and leptons considered in Section 3:

$$p_{l_n} = \frac{m_{ll}^{\max} m_{ql_n}^{\max}}{2m_{ql_f}^{\max}}, \quad (5.5)$$

$$p_q = \frac{m_{ql_n}^{\max} m_{ql_f}^{\max}}{2m_{ll}^{\max}}, \quad (5.6)$$

$$p'_{l_f} = \frac{m_{ql_f}^{\max(0)} m_{ll}^{\max}}{2m_{ql_n}^{\max}}. \quad (5.7)$$

6. Detector-level study

6.1 Introduction

Having outlined some possible sparticle mass measurement strategies making use of the additional information provided by invariant mass correlations we now illustrate how such strategies may be used in practice with detector-level events. Although a very wide range of new variables are potentially now available we shall concentrate on a small subset representing a limited evolution of the conventional global end-point technique. This will enable us to highlight the main benefit of the new technique, namely the ambiguity resolution discussed in Section 5, without compromising event statistics near the end-points.

We shall focus purely on m_{qll} and m_{ql} end-points as functions of m_{ll} in order to minimise the possibility of under-estimating statistical uncertainties through the presence of correlations between end-point observables. Such correlations could arise if the same events appear at the end-points of two or more invariant mass distributions. Estimation of these correlations is beyond the scope of the current paper and so we choose instead to minimise their effects by judicious selection of minimally correlated observables. With more work to understand such correlations further improvements in mass measurement precision could potentially be obtained.

It should be noted that throughout this section we consider end-points in distributions of invariant masses rather than squared invariant masses. The use of the former here enables comparison of results with those of previous studies, and is consistent with the discussion of Section 5.

6.2 Event simulation, selection and reconstruction

The 100 fb^{-1} equivalent sample of SPS1a events described in Section 2.1 was passed through a fast simulation of a generic LHC detector [22]. In addition a 100 fb^{-1} equivalent sample of $t\bar{t}$ background events was generated with `HERWIG 6.4` [18], passed through the same fast detector simulation, filtered to require at least two leptons (e or μ) and added to the signal sample. $t\bar{t}$ events are expected to form the dominant SM background to the analysis described here, however the event selection and background subtraction described below are found to reduce this contribution to negligible levels (typically $\lesssim 10$ events for 100 fb^{-1} of data).

Events were selected with the same requirements as were used in Ref. [17] to aid comparison:

- At least four jets with the hardest three satisfying: $p_T(j_1) > 150$ GeV, $p_T(j_2) > 100$ GeV, $p_T(j_3) > 50$ GeV
- $M_{\text{eff}} = E_T^{\text{miss}} + p_T(j_1) + p_T(j_2) + p_T(j_3) + p_T(j_4) > 600$ GeV
- $E_T^{\text{miss}} > \max(100\text{GeV}, 0.2M_{\text{eff}})$
- Exactly two isolated opposite-sign same-flavour (OSSF) leptons (e/μ) satisfying: $p_T(l_1) > 20$ GeV, $p_T(l_2) > 10$ GeV.

Following event selection the invariant mass of the OSSF lepton pair (m_{ll}) was calculated for each event. The m_{ll} distribution of events containing opposite-sign opposite-flavour (OSOF) lepton pairs was subtracted from that of OSSF events in order to remove SM and SUSY background events containing uncorrelated leptons. The resulting m_{ll} distribution is shown in Figure 8(top). This OSOF subtraction procedure was also applied when generating all of the invariant mass distributions shown below. These distributions also all require that $m_{ll} < 80$ GeV (3 GeV above the observed value of m_{ll}^{max}).

The next step in the analysis involves indentifying the hard jet generated by the assumed decay chain Eqn. (2.2). Throughout this analysis this jet was assumed to be one of the two leading jets in the event. When calculating the maxima of invariant mass distributions this jet was further assumed conservatively to be the one which minimises m_{qll} , while when calculating thresholds and invariant mass ratios the jet which maximises m_{qll} was used. This latter m_{qll} value is referred to as $m_{qll(\text{hi})}$ below. When calculating m_{ql} end-points only those events in which the two possible m_{qll} values lie either side of the observed m_{qll}^{max} end-point were used. When calculating distributions of ratios of invariant masses this requirement was strengthened to require that both m_{qll} values lie below the observed m_{qll}^{max} end-point.

6.3 Global end-point analysis

The integrated m_{qll} , $m_{qll(\text{hi})}$, $m_{ql(\text{lo})}$ and $m_{ql(\text{hi})}$ distributions obtained from this analysis are shown in the bottom four panels of Figure 8 and agree well with the results of earlier work [17]. These distributions were fitted with linear functions to determine the positions of the global end-points while the m_{ll} distribution (Figure 8(top)) was fitted with a ‘triangular’ distribution smeared with a gaussian resolution function of variable width, as described in e.g. Ref. [2]. A more detailed analysis might involve fitting with the analytical functions described in Ref. [4] or simulated detector-level template distributions, however such developments are beyond the scope of this paper.

The mean end-point positions and their associated statistical uncertainties obtained from the fits are shown in Table 1. The agreement between the nominal end-point positions expected from the masses used in the **HERWIG** generator and the fitted means is reasonable in all cases. Also shown in Table 1 are the jet/lepton energy scale (JES and LES) systematic uncertainties, assumed to be 1% and 0.1% respectively. The scale uncertainties in the m_{ql} and m_{qll} end-points are dominated by the JES uncertainty leading to a 100% correlation between the systematic uncertainties in these observables. As discussed in Ref. [17]

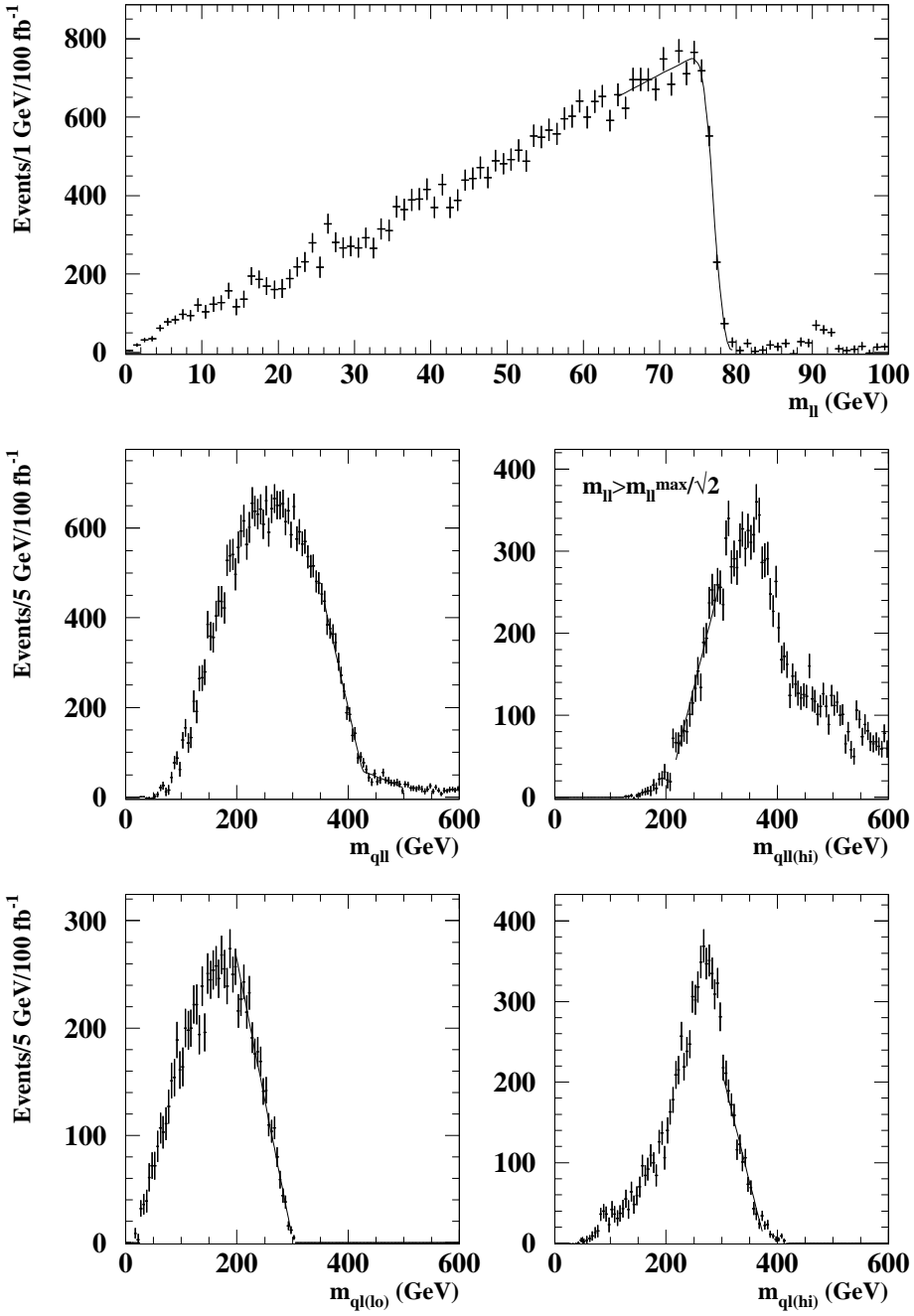


Figure 8: Detector-level invariant mass distributions for the SPS1a benchmark SUSY model used in the conventional integrated end-point analysis.

the systematic uncertainties arising from variation of input parameters in these naive fits are potentially significant ($\lesssim 10$ GeV) however for the purposes of this analysis we shall henceforth neglect these systematics.

Observable	Input	Mean	Statistical error	Energy scale error
m_{ll}^{\max}	77.053	77.006	0.057	0.077
m_{qll}^{\max}	428.4	425.3	1.8	4.3
m_{qll}^{\min}	201.8	200.8	3.1	2.0
$m_{ql(hi)}^{\max}$	377.9	378.0	1.6	3.8
$m_{ql(lo)}^{\max}$	300.2	301.3	1.0	3.0

Table 1: Summary of measurements of end-points in integrated invariant mass distributions for the SPS1a benchmark SUSY model. states. Column 2 lists the end-point positions expected from the masses used in the `HERWIG` generator while Columns 3 and 4 provide the fitted end-point positions. Column 5 provides the systematic uncertainty obtained from jet and lepton energy scale uncertainties of 1% and 0.1% respectively. All masses are in GeV.

In order to determine the precision with which individual sparticle masses can be measured with the global end-point constraints listed above, 10000 LHC experiments were simulated with a simple toy Monte Carlo code. For each MC experiment values for each of the end-point positions were drawn from gaussian distributions centred on the nominal values with widths determined by the uncorrelated statistical and correlated systematic scale uncertainties listed in Table 1. The end-point positions were then fitted with the formulae listed in Section 2.2 (Eqns. (2.3), (2.7), (2.9) and (2.10)) using `MINUIT` [23]. The χ^2 minimisation function which was used was that described in Refs. [2, 3]:

$$\chi^2 = [\mathbf{E}^{\text{exp}} - \mathbf{E}^{\text{th}}(\mathbf{m})]^T \mathbf{W} [\mathbf{E}^{\text{exp}} - \mathbf{E}^{\text{th}}(\mathbf{m})], \quad (6.1)$$

where \mathbf{E}^{exp} and $\mathbf{E}^{\text{th}}(\mathbf{m})$ are vectors of respectively observed and predicted end-point positions (the latter functions of the vector of sparticle masses \mathbf{m}), and the weight matrix \mathbf{W} is the inverse of the correlation matrix of the end-point observables. This form of the minimisation function takes into account, through the use of \mathbf{W} , the correlations between m_{qll} and m_{ql} end-point observables generated by the correlated JES systematic uncertainties.

As discussed in Ref. [3], excluding the m_{qll}^{\min} constraint generates a two-fold ambiguity in the allowed set of mass values for the SPS1a model, corresponding to cases A1 and A2 in Eqn. (2.7). To properly account for this ambiguity we performed the fit twice for each MC experiment, with the initial values of the four masses set to the analytical solutions given by these two cases, listed in Ref. [3]. The solution with the minimum χ^2 value was then selected.

The distributions of fitted mass values obtained from the 10000 toy MC experiments are shown in Figure 9, which also provides the means and RMS values of the distributions. The latter provide estimates of the sparticle mass measurement precisions. Also shown in the Figure are the distributions of mass solutions obtained by starting the fits from each of the two sets of analytical formulae corresponding to cases A1 and A2. The incorrect solution corresponding to case A2 contributes 32% of solutions and generates mass values ~ 10 GeV below the nominal values. It can clearly be seen that these incorrect solutions significantly decrease the precision with which the masses can be measured.

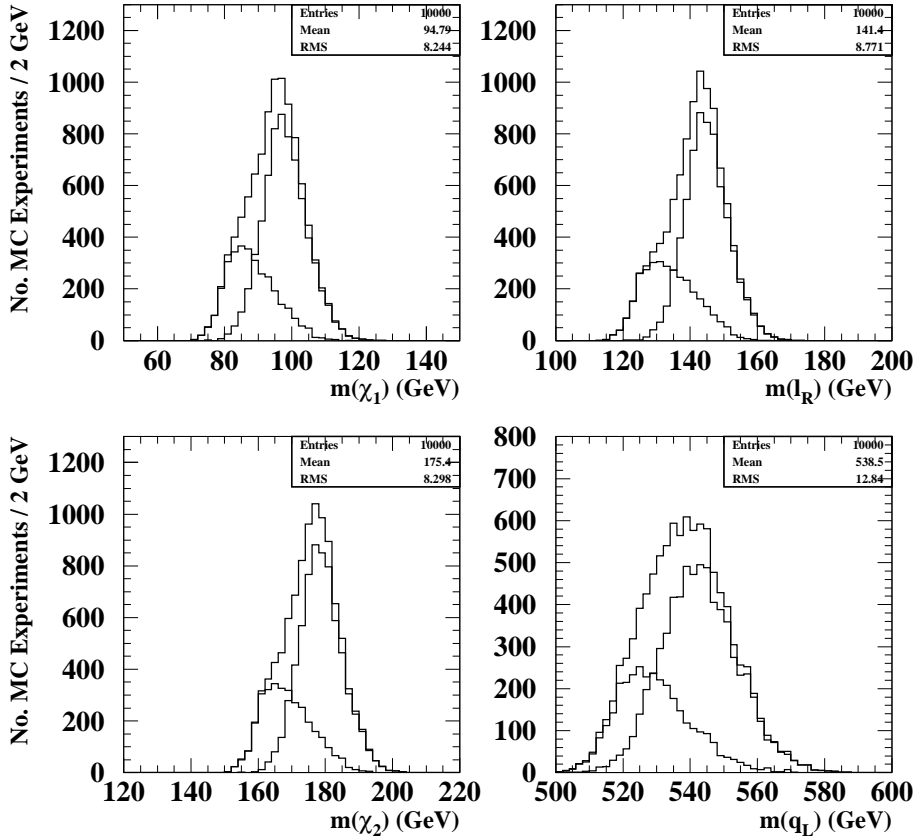


Figure 9: Fitted sparticle masses for the SPS1a benchmark SUSY model obtained from the conventional global end-point analysis. In each case the two smaller histograms underlying the large (sum) histogram represent the distributions obtained by using the analytical mass formulae for cases A2 (left - incorrect assumption for SPS1a) and A1 (right - correct assumption for SPS1a). The latter distributions possess widths ranging from 6.6 GeV ($m_{\tilde{\chi}_1^0}$) to 11.3 GeV ($m_{\tilde{q}_L}$).

6.4 Conditional end-point analysis

When exploiting invariant mass correlations with conditional end-points we start by confirming that the selected events do indeed contain sequential two-body lepton-producing decays. In the global end-point analysis this can be accomplished by studying the shape of the m_{ll} distribution (Figure 8(top)), which departs from the canonical ‘smeared triangle’ when the dilepton pair is produced off mass-shell (see e.g. Ref. [21]). This shape analysis potentially requires large event statistics and a good understanding of detector performance to conclusively exclude the three-body hypothesis however, since the latter is effectively the off mass-shell limit of the sequential two-body case. With invariant mass correlations however we can also plot the reconstructed ratio $m_{ql(hi)}/m_{ql(lo)}$ for small m_{ll} discussed in Section 4.3. This is plotted in Figure 10 at detector-level for $m_{ll} < 10$ GeV. Comparison

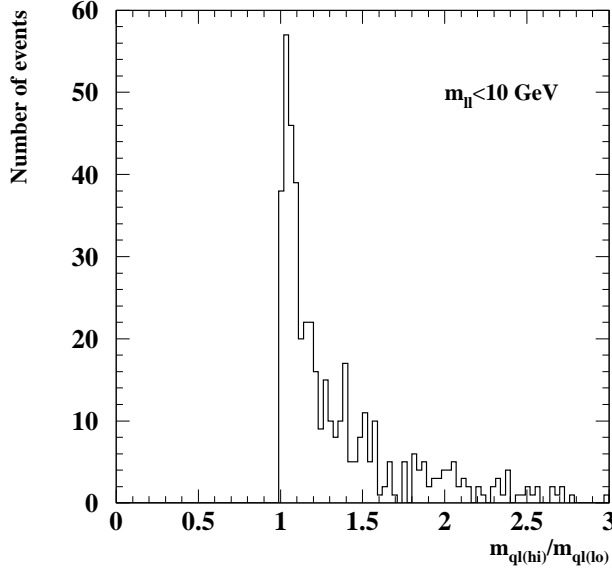


Figure 10: Distribution of the detector-level ratio $m_{ql(hi)}/m_{ql(lo)}$ for $m_{ll} < 10$ GeV for the SPS1a benchmark SUSY model.

with Figure 7 shows that the prominent peak associated with sequential two-body lepton-producing decays has survived detector-level smearing and the application of selection cuts and hence this distribution provides clear evidence for such decay chains.

The next step in the analysis involves identifying whether $m_{ql(hi)}^{\max}$ measures $m_{ql_f}^{\max}$ or $m_{ql_n}^{\max}$, i.e. whether cases A1/A2 or A3 in Eqn. (2.7) are correct. To accomplish this we construct two $m_{ql(hi)}$ distributions (Figure 11) – one for events with low m_{ll} (< 30 GeV) and one for the remaining events (30 GeV $< m_{ll} < m_{ll}^{\max}$). Fitting the end-points $m_{ql(hi)}^{\max(m_{ll})}$ of these distributions with simple linear functions we find that their positions differ significantly (see Table 2). This confirms that the value of $m_{ql(hi)}^{\max}$ used in the global end-point analysis measures $m_{ql_f}^{\max}$, as does the larger of the two $m_{ql(hi)}^{\max(m_{ll})}$ end-points measured here. The smaller of the two $m_{ql(hi)}^{\max(m_{ll})}$ end-points can then be used with Eqn. (4.4) to determine $m_{ql_f}^{\max(0)}$ as described in Section 5.

Having excluded case A3 from Eqn. (2.7) we now aim to measure $m_{ql_n}^{\max}$ unambiguously, which will help us to resolve the A1/A2 ambiguity in $m_{ql(lo)}^{\max}$. To do this we construct the distribution of m_{ql} , where each selected event contributes two entries ($m_{ql(hi)}$ and $m_{ql(lo)}$). We further require that m_{ll} be large (70 GeV $< m_{ll} < m_{ll}^{\max}$) in order to maximise the separation between the conditional upper bound on $m_{ql(hi)}$ provided by $m_{ql_f}^{\max(m_{ll})}$, at the lower end of the m_{ll} range, and the ‘hidden’ end-point measuring $m_{ql_n}^{\max}$, whose position is independent of m_{ll} . The value of $m_{ql_f}^{\max(m_{ll})}$ at the lower end of the m_{ll} range determines the value of m_{ql} at which the distribution begins to fall off \sim linearly towards $m_{ql_f}^{\max}$.

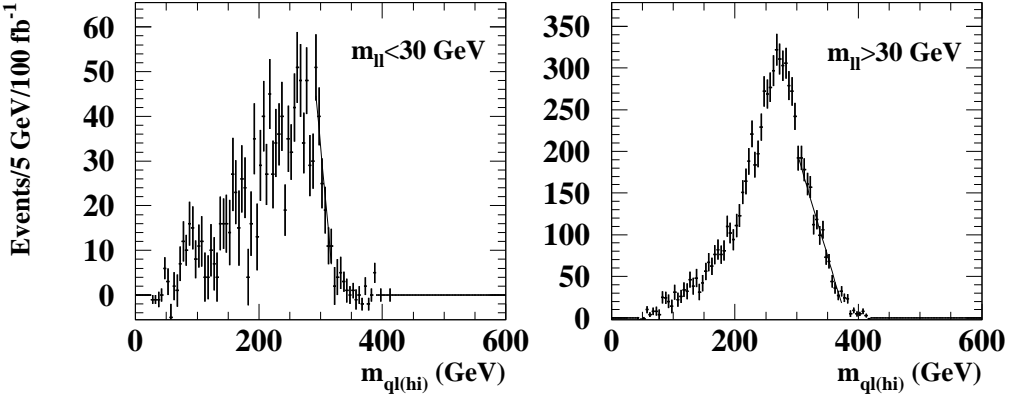


Figure 11: Detector-level $m_{ql(hi)}$ distributions for the SPS1a benchmark SUSY model for $m_{ll} < 30$ GeV (left) and $m_{ll} > 30$ GeV (right).

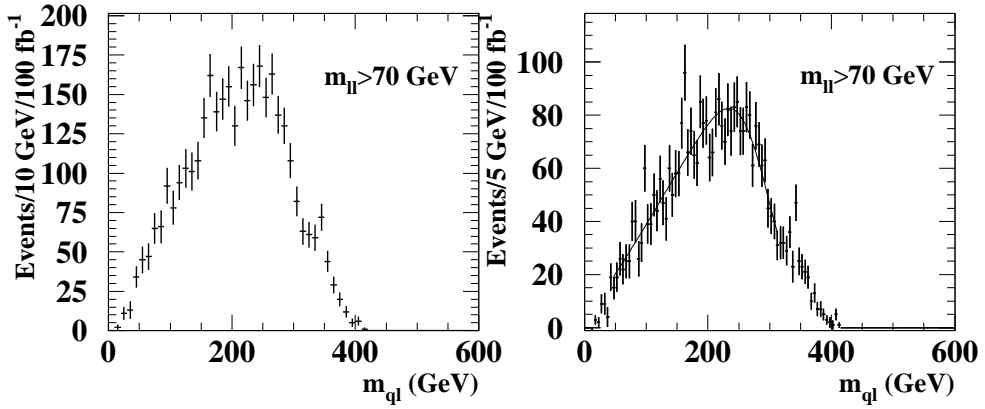


Figure 12: Detector-level m_{ql} distribution for the SPS1a benchmark SUSY model for $m_{ll} > 70$ GeV (left) and showing end-point fit (right). The same distribution is plotted in the left-hand figure as the right-hand figure but with twice the bin-width to improve the visibility of the m_{ql_n} end-point.

Consequently by maximising the separation of this $m_{ql_f}^{\max(m_{ll})}$ value from the $m_{ql_n}^{\max}$ end-point we maximise the visibility of the latter. The resulting m_{ql} distribution is shown in Figure 12 and displays both the linear end-point expected from $m_{ql_f}^{\max(m_{ll})}$ at 340 – 380 GeV and the hidden $m_{ql_n}^{\max}$ end-point at ~ 300 GeV. The lack of dependence of the $m_{ql_n}^{\max}$ end-point on m_{ll} causes it to have the same characteristic ‘triangular’ shape as the m_{ll}^{\max} end-point at parton-level and consequently we fit this distribution with the same ‘smeared triangle’ used to determine the m_{ll}^{\max} end-point position. The fit results are shown in

Observable	m_{ll} (low)	m_{ll} (high)	Input	Mean	Statistical error	Energy scale error
m_{ll}^{\max}	—	—	77.053	77.006	0.057	0.077
$m_{ql}^{\max(m_{ll})}$	0.0	70.0	428.4	434.9	1.4	4.3
$m_{ql}^{\max(m_{ll})}$	70.0	m_{ll}^{\max}	401.6	400.0	3.7	4.0
m_{ql}^{\min}	$m_{ll}^{\max}/\sqrt{2}$	m_{ll}^{\max}	201.8	200.8	3.1	2.0
$m_{ql}^{\max(m_{ll})}$	0.0	30.0	317.6	322.1	3.2	3.2
$m_{ql}^{(hi)}$	30.0	m_{ll}^{\max}	377.9	379.6	1.8	3.8
$m_{ql}^{\max(m_{ll})}$	70.0	m_{ll}^{\max}	300.2	295.4	2.7	3.0
$m_{ql}^{\max(m_{ll})}$	0.0	70.0	300.2	300.5	1.2	3.0
$m_{ql}^{\max(m_{ll})}$	70.0	m_{ll}^{\max}	268.3	268.1	2.6	2.7

Table 2: Summary of measurements of end-points in conditional invariant mass distributions for the SPS1a benchmark SUSY model. Columns 2 and 3 provide the m_{ll} ranges over which the invariant mass distributions are integrated to give the conditional end-points listed in Column 1. Column 4 lists the end-point positions expected from the masses used in the **HERWIG** generator while Columns 5 and 6 provide the fitted end-point positions and statistical uncertainties. Column 7 provides the systematic uncertainty obtained from jet and lepton energy scale uncertainties of 1% and 0.1% respectively. All masses are in GeV.

Table 2. The visibility of the hidden m_{qln}^{\max} end-point may be less clear if a more realistic detector simulation is used, however more detailed studies of the m_{ql} distribution over the full m_{ll} range may corroborate an ambiguous observation in this case. Henceforth we shall therefore assume that an unambiguous measurement can be obtained.

With the extra information provided by the m_{qln}^{\max} end-point we should potentially be able to resolve the A1/A2 ambiguity in m_{ql}^{\max} . Rather than simply measuring the value of the global $m_{ql}^{(lo)}$ bound however we proceed by measuring the value of the conditional bound $m_{ql}^{\max(m_{ll})}$ in two m_{ll} bins: $0 < m_{ll} < 70$ GeV and $70 \text{ GeV} < m_{ll} < m_{ll}^{\max}$. The first bin contains the global end-point $m_{ql}^{(lo)}$ (which for SPS1a measures m_{qln}^{\max} via case A1) while the second provides a measure of the shape of the upper bound on $m_{ql}^{(lo)}$ determined by Eqn. (4.6). The $m_{ql}^{(lo)}$ distributions in these bins are shown in Figure 13 and the results of linear end-point fits are listed in Table 2. Of course we do not know *a priori* how to interpret these end-points, however by using these measurements as constraints in the subsequent global mass fit the correct interpretation can be determined with the help of the other end-point measurements, particularly m_{qln}^{\max} .

We also measure the conditional bound $m_{qll}^{\max(m_{ll})}$ in the same two m_{ll} bins used above to measure $m_{ql}^{\max(m_{ll})}$. The two m_{qll} distributions are shown in Figure 14 while the results of linear end-point fits are listed in Table 2. The $m_{qll}^{\max(m_{ll})}$ end-point observed in the first bin lies at the position of the global m_{qll} end-point m_{qll}^{\max} while the end-point in the second bin provides a measure of $m_{qll}^{\max(m_{ll})}$ determined by Eqn. (4.3).

In addition to the above end-point constraints we make use of the m_{ll}^{\max} and m_{ll}^{\min} constraints from the global end-point analysis. When added to the end-point constraints discussed above this gives nine end-point constraints, listed in Table 2. In most cases there is reasonable agreement between the fitted means and the nominal end-point positions.

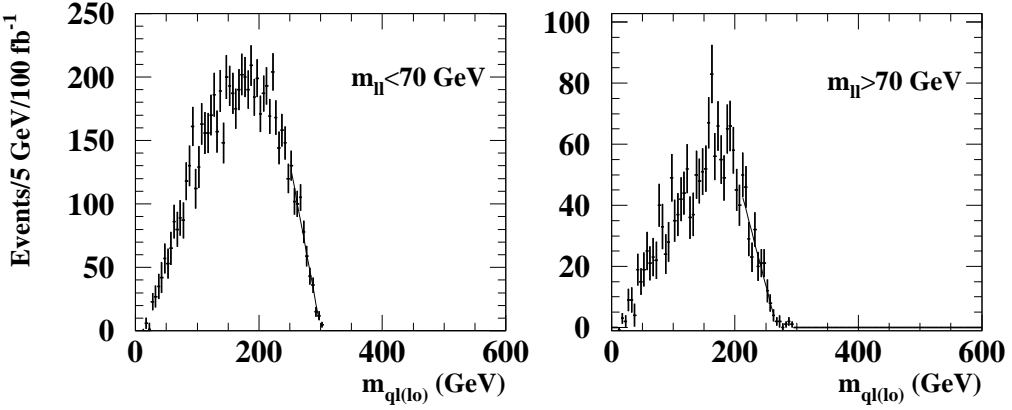


Figure 13: Detector-level $m_{ql(lo)}$ distributions for the SPS1a benchmark SUSY model for $m_{ll} < 70$ GeV (left) and $m_{ll} > 70$ GeV (right).

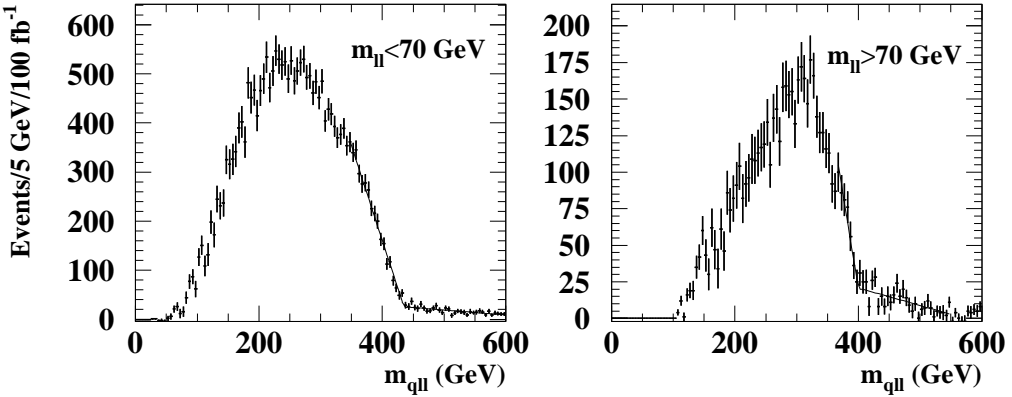


Figure 14: Detector-level m_{qll} distributions for the SPS1a benchmark SUSY model for $m_{ll} < 70$ GeV (left) and $m_{ll} > 70$ GeV (right).

The fitted position of the first $m_{qll}^{\max(m_{ll})}$ end-point departs from the nominal position by 4.6σ indicating that more work is needed to define the fitting function in this case, however this will not be considered further here.

As in the global end-point analysis the precision with which SUSY particle masses can be measured was determined by generating 10000 toy MC experiments in which the end-point positions were smeared from their nominal values with gaussians with widths determined by the appropriate uncorrelated statistical and correlated systematic scale uncertainties. A global fit to the end-point constraints was then performed with the formulae from Sections 2.2 and 4.2 as described in Section 6.3. The initial values of the sparticle

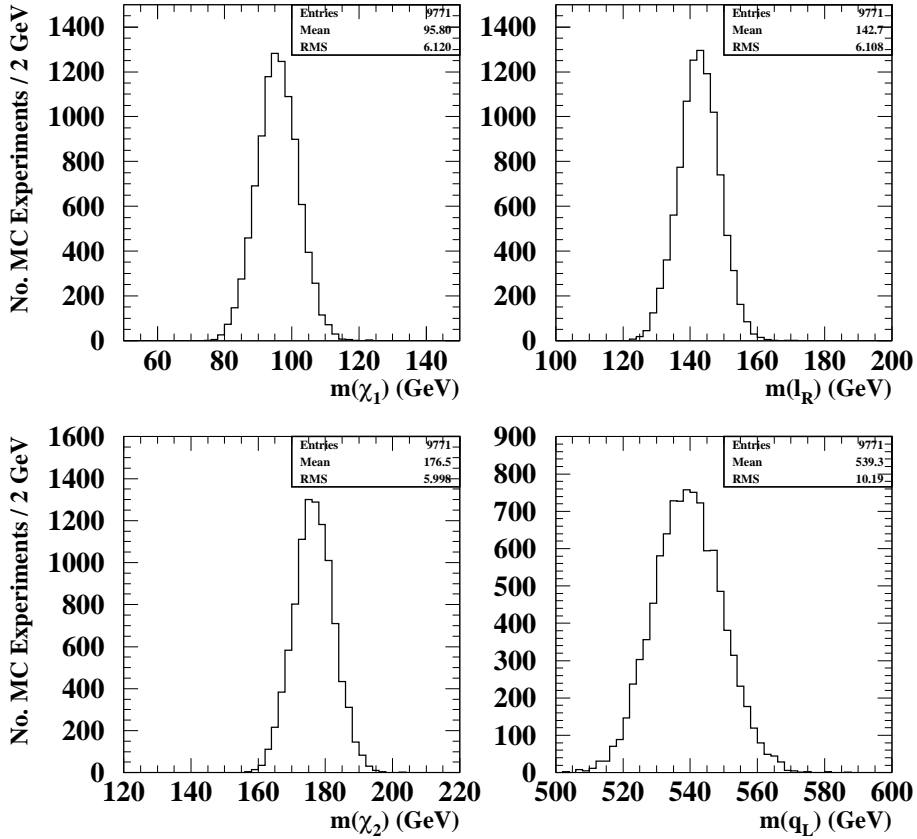


Figure 15: Fitted sparticle masses for the SPS1a benchmark SUSY model obtained from the conditional end-point analysis using invariant mass correlations.

masses used in the fits were determined by calculating m_{qlf}^{\max} (given by the larger $m_{ql(hi)}^{\max(m_{ll})}$ end-point), $m_{qlf}^{\max(0)}$ (obtained from the two $m_{ql(hi)}^{\max(m_{ll})}$ end-points), m_{qln}^{\max} and m_{ll}^{\max} and then using Eqns. (5.1)–(5.4).

The distributions of sparticle masses obtained from the 10000 MC experiments are listed in Figure 15. The means and RMS values of these distributions are compared with the equivalent quantities from the global end-point analysis in Table 3. The distributions obtained from the conditional end-point analysis are $\sim 20\%-30\%$ narrower, and also less skewed, than those obtained using global end-points, primarily due to resolution of the A1/A2 ambiguity but also due to the use of additional end-point constraints. It should be noted however that as in the case of the global end-point analysis the conditional end-point analysis does not establish the identities of the intermediate states, merely their masses.

7. Conclusions

This paper has shown that additional constraints on sparticle masses at the LHC can be

State	Input	Global end-point fit		Conditional end-point fit	
		Mean	Error	Mean	Error
$\tilde{\chi}_1^0$	96.05	94.8	8.2	95.8	6.1
\tilde{l}_R	142.97	141.4	8.8	142.7	6.1
$\tilde{\chi}_2^0$	176.81	175.4	8.3	176.5	6.0
\tilde{q}_L	540.0	538.5	12.8	539.3	10.2

Table 3: Summary of sparticle mass measurement precisions for SPS1a states. Column 2 lists input masses used in the toy MC simulation, Columns 3 and 4 the fitted masses and uncertainties obtained from the conventional global end-point analysis and Columns 5 and 6 the equivalent values obtained from the conditional end-point fit. All masses are in GeV.

obtained by exploiting correlations between invariant mass end-points obtained from the sequential two-body decay chains used in the conventional global end-point analysis. The same techniques can also be used to confirm that selected events contain sequential two-body lepton-producing decays rather than three-body decays. These additional constraints can be used to improve the precision with which sparticle masses can be measured, although care must be taken to account for any correlations between end-point positions.

The results of this paper indicate a number of potential avenues for future work. Most importantly a detailed detector-level Monte Carlo study of a large number of experiments should be performed to determine the level of correlation between different end-point observables. With a more detailed understanding of such correlations more constraints could be used than in the simple study described here, leading to further improvements in mass measurement precision. In addition it would be profitable to calculate analytical formulae for the end-point shapes similar to those for the global end-points described in Ref. [4].

Acknowledgements

The authors wish to thank Giacomo Polesello for helpful comments on a draft of this paper and for providing the simulated datasets on which the work was based. They also wish to thank Chris Lester for further helpful comments. DRT and DC wish to acknowledge STFC for support.

Appendix A: Three-body lepton-producing decay chains

For completeness we list here some formulae for kinematic bounds equivalent to those listed in Section 4, for three-body lepton-producing decay chains incorporating single two-body quark-producing decays of the form:

$$\tilde{q}_L \rightarrow \tilde{\chi}_2^0 q \rightarrow \tilde{\chi}_1^0 l_1 l_2 q. \quad (\text{A1})$$

The global end-points from such decay chains in NUHM models were considered in Ref. [21].

The m_{qll} bound as a function of m_{ll} in this case is identical to that for the two-body case listed in Eqn. (4.3). The $m_{ql(\text{hi})}$ bound as a function of m_{ll} equivalent to Eqns. (4.4) and (4.5) can also be obtained from Eqn. (4.3) by recognising that $m_{ql(\text{hi})}$ is maximised

when the $\tilde{\chi}_1^0$, q and one of the leptons are all co-linear in the rest frame of the $\tilde{\chi}_2^0$. In this case one of the two lepton+quark invariant masses is zero and hence

$$(m_{ql(\text{hi})}^{\text{bound}(m_{ll})})^2 = (m_{qll}^{\text{bound}(m_{ll})})^2 - m_{ll}^2 \quad (\text{A2})$$

$$= \frac{(m_{\tilde{q}L}^2 - m_{\tilde{\chi}_2^0}^2)}{2m_{\tilde{\chi}_2^0}^2} \left(m_{\tilde{\chi}_2^0}^2 - m_{\tilde{\chi}_1^0}^2 + m_{ll}^2 \pm \sqrt{\lambda(m_{\tilde{\chi}_2^0}, m_{\tilde{\chi}_1^0}, m_{ll})} \right). \quad (\text{A3})$$

This is maximised when $m_{ll} = 0$, which gives the position of the global end-point reported in Ref. [21]:

$$(m_{ql(\text{hi})}^{\text{max}})^2 = \frac{(m_{\tilde{q}L}^2 - m_{\tilde{\chi}_2^0}^2)(m_{\tilde{\chi}_2^0}^2 - m_{\tilde{\chi}_1^0}^2)}{m_{\tilde{\chi}_2^0}^2}, \quad (\text{A4})$$

while if $m_{ll} = m_{ll}^{\text{max}} = m_{\tilde{\chi}_2^0} - m_{\tilde{\chi}_1^0}$ then

$$(m_{ql(\text{hi})}^{\text{max}(m_{ll})})^2 = \frac{(m_{\tilde{q}L}^2 - m_{\tilde{\chi}_2^0}^2)(m_{\tilde{\chi}_2^0}^2 - m_{\tilde{\chi}_2^0}m_{\tilde{\chi}_1^0})}{m_{\tilde{\chi}_2^0}^2}. \quad (\text{A5})$$

The $m_{ql(\text{lo})}$ bound equivalent to that derived from Eqn. (4.6) can be obtained from the three-body analogue of Eqn. (3.12) by conserving energy and momentum in the qll plane. This equation is more complicated than Eqn. (3.12) but setting $m_{ql1} = m_{ql2}$ it simplifies considerably to give:

$$(m_{ql(\text{lo})}^{\text{bound}(m_{ll})})^2 = \frac{(m_{\tilde{q}L}^2 - m_{\tilde{\chi}_2^0}^2)}{4m_{\tilde{\chi}_2^0}^2} \left(m_{\tilde{\chi}_2^0}^2 - m_{\tilde{\chi}_1^0}^2 + m_{ll}^2 \pm \sqrt{\lambda(m_{\tilde{\chi}_2^0}, m_{\tilde{\chi}_1^0}, m_{ll})} \right) \quad (\text{A6})$$

$$= \frac{(m_{ql(\text{hi})}^{\text{bound}(m_{ll})})^2}{2}. \quad (\text{A7})$$

Consequently the $m_{ql(\text{hi})}$ bound is $\sqrt{2}$ times as large as the $m_{ql(\text{lo})}$ bound, as was noted for the global maximum in Ref. [21].

References

- [1] I. Hinchliffe, F. E. Paige, M. D. Shapiro, J. Soderqvist and W. Yao, Phys. Rev. D **55** (1997) 5520 [arXiv:hep-ph/9610544].
- [2] B. C. Allanach, C. G. Lester, M. A. Parker and B. R. Webber, JHEP **0009** (2000) 004 [arXiv:hep-ph/0007009].
- [3] B. K. Gjelsten, D. J. Miller and P. Osland, JHEP **0412** (2004) 003 [arXiv:hep-ph/0410303].
- [4] D. J. Miller, P. Osland and A. R. Raklev, JHEP **0603** (2006) 034 [arXiv:hep-ph/0510356].
- [5] C. G. Lester and D. J. Summers, Phys. Lett. B **463** (1999) 99 [arXiv:hep-ph/9906349].
- [6] A. Barr, C. Lester and P. Stephens, J. Phys. G **29** (2003) 2343 [arXiv:hep-ph/0304226].
- [7] W. S. Cho, K. Choi, Y. G. Kim and C. B. Park, arXiv:0709.0288 [hep-ph].

- [8] D. R. Tovey, JHEP **0804** (2008) 034 [arXiv:0802.2879 [hep-ph]].
- [9] B. Gripaios, JHEP **0802** (2008) 053 [arXiv:0709.2740 [hep-ph]].
- [10] A. J. Barr, B. Gripaios and C. G. Lester, arXiv:0711.4008 [hep-ph].
- [11] W. S. Cho, K. Choi, Y. G. Kim and C. B. Park, arXiv:0711.4526 [hep-ph].
- [12] H. C. Cheng, J. F. Gunion, Z. Han, G. Marandella and B. McElrath, arXiv:0707.0030 [hep-ph].
- [13] M. M. Nojiri, G. Polesello and D. R. Tovey, JHEP **0805** (2008) 014 [arXiv:0712.2718 [hep-ph]].
- [14] P. Huang, N. Kersting and H. H. Yang, arXiv:0802.0022 [hep-ph].
- [15] M. Bisset, R. Lu and N. Kersting, arXiv:0806.2492 [hep-ph].
- [16] B. C. Allanach *et al.*, in *Proc. of the APS/DPF/DPB Summer Study on the Future of Particle Physics (Snowmass 2001)* ed. N. Graf, *In the Proceedings of APS / DPF / DPB Summer Study on the Future of Particle Physics (Snowmass 2001), Snowmass, Colorado, 30 Jun - 21 Jul 2001, pp P125* [arXiv:hep-ph/0202233].
- [17] B.K. Gjelsten, J. Hisano, K. Kawagoe, E. Lytken, D. Miller, M. M. Nojiri, P. Osland and G. Polesello in G. Weiglein *et al.* [LHC/LC Study Group], Phys. Rept. **426** (2006) 47 [arXiv:hep-ph/0410364].
- [18] G. Corcella *et al.*, JHEP **0101** (2001) 010 [arXiv:hep-ph/0011363].
- [19] S. Moretti, K. Odagiri, P. Richardson, M. H. Seymour and B. R. Webber, JHEP **0204** (2002) 028 [arXiv:hep-ph/0204123].
- [20] C. G. Lester, PhD Thesis, University of Cambridge, December 2001.
- [21] C. G. Lester, M. A. Parker and M. J. . White, JHEP **0710** (2007) 051 [arXiv:hep-ph/0609298].
- [22] E. Richter-Was, arXiv:hep-ph/0207355.
- [23] F. James and M. Roos, Comput. Phys. Commun. **10** (1975) 343.